Supporting Information for

Deformation mechanisms and remarkable strain hardening in single-crystalline high-entropy-alloy micro/nanopillars

Qian Zhang[1], Ruirui Huang[1], Xuan Zhang[1], Tangqing Cao[2], Yunfei Xue[2], Xiaoyan Li[1*]

[1]Center for Advanced Mechanics and Materials, Applied Mechanics Laboratory, Department of Engineering Mechanics, Tsinghua University, Beijing 100084, China

[2]School of Materials Science and Engineering, Beijing Institute of Technology, Beijing 100081, China

*Corresponding author. Email: xiaoyanlithu@tsinghua.edu.cn.

This PDF file includes:

Video S2. In situ compression of [110]-oriented nanopillar with diameter of 1015 nm.

Video S3. In situ compression of [111]-oriented nanopillar with diameter of 1239 nm.

Video S4. Atomistic simulation of uniaxial compression on [100]-oriented nanopillar with diameter of 30 nm.

Video S5. Atomistic simulation of uniaxial compression on [110]-oriented nanopillar with diameter of 30 nm.

Video S6. Atomistic simulation of uniaxial compression on [111]-oriented nanopillar with diameter of 30 nm.

Video S7. Dislocation evolution during uniaxial compression on [100]-oriented nanopillar with diameter of 30 nm.

Video S8. Dislocation evolution during uniaxial compression on [110]-oriented nanopillar with diameter of 30 nm.

Video S9. Dislocation evolution during uniaxial compression on [111]-oriented nanopillar with diameter of 30 nm.

AlCrFeCoNi interatomic potential table. The embedded atom method potential describing the self- and cross-interactions of Al-Cr-Fe-Co-Ni.

Methods

Sample preparation and microstructural characterization. The AlCrFeCoNi bulk samples were fabricated through arc melting Al, Cr, Fe, Co, and Ni powders (>99.9% purity) with equiatomic concentrations under an argon atmosphere. During fabrication, the ingots were triple melted to ensure chemical homogenization. The alloy ingots were cast into a copper mold with dimensions of $16 \times 20 \times 80$ mm^3. To reduce elemental segregation and obtain equiaxed grain structures, the as-cast alloys were heated at 1000 ℃ for 24 h followed by water cooling. The lattice constant and phase compositions of the sample were determined by the X-ray diffraction (XRD). The electron backscattered diffraction (EBSD) and energy dispersive spectrum (EDS) techniques were used to characterize the distribution of the grain orientations and element compositions using a scanning electron microscopy (SEM) (FEI Nova Nano430). According to the orientation mapping, we selected several grains with orientations of [100], [110] and [111] and then fabricated single-crystalline pillars within these grains using a focused ion beam (FIB)-SEM system (LYRA3 TESCAN). The pillars were milled by using a voltage and current of 30 kV and 1 nA and by final polishing with a voltage and current of 30 kV and 50 pA, respectively. The diameter of the fabricated pillar varied from 270 nm to 1,583 nm. All pillars showed a taper of less than $3°$ and aspect ratios varying from 2.5 to 3.5. The samples used for transmission electron microscopy (TEM) observations were fabricated using a Hitachi FB2200 FIB. The pillars were sputtered with tungsten for protection before FIB milling. Microstructural observations were conducted by using a JEM-2100F TEM with an accelerating voltage of 300 keV.

In-situ SEM compressive tests. In-situ uniaxial compressive tests were conducted at room temperature inside a SEM (Quanta FEG450) equipped with a Hysitron PicoIndenter 85. A diamond flat punch with a diameter of 5 μm was used. All specimens were compressed to a total strain of approximately 60% at a constant strain rate of 1.3×10^{-3} s^{-1}.

Nanoindentation tests. Nanoindentation tests were conducted on several selected large grains with orientations of [100], [110] and [111] in bulk samples by using a

Hysitron TI950 with a Berkovich indenter. For each orientation, we conducted 8 nanoindentation tests. The moduli for the indented samples were extracted based on the Oliver-Pharr model[1].

Atomistic simulations. To complement the experiments and reveal the underlying deformation mechanisms, we performed a series of large-scale atomistic simulations for uniaxial compression of AlCrFeCoNi nanopillars via a large-scale atomic/molecular massively parallel simulator (LAMMPS)[2]. The atomic configurations for the HEA samples with [100], [110] and [111] orientations were constructed by first building the Cr single crystal and then randomly replacing Cr atoms in a single crystal with the other four elemental atoms while ensuring equiatomic concertation. The constructed HEA single crystal is sufficiently large so that it can be cut into nanopillars with a diameter of 30 nm and an aspect ratio of 3.0. Using a recently developed embedded atom method (EAM) potential database[3], we constructed an EAM potential for a quinary alloy (i.e., AlCrFeCoNi). The table of this potential is given in the Supporting Information. During simulations, this potential was used to describe the interatomic interaction for HEA samples. This potential is capable of accurately predicting the microstructures (such as lattice structure, phase, short-range order and chemical cluster) and structural/mechanical properties (such as modulus, surface energy, and stacking fault energy) of various conventional alloys[3-5]. We conducted some preliminary molecular dynamics (MD) simulations to check the reliability and accuracy of this potential for Al_xCrFeCoNi samples. Figures S4a-b show the variation of the BCC lattice constants and Young's moduli for Al_xCrFeCoNi with Al content x. It is seen that the predictions based on MD simulations are in good agreement with previous experimental[6-10] and simulation results[11]. This indicates that this potential can predict the lattice constants, moduli and stable phase for Al_xCrFeCoNi (x>1.0). All nanopillars were equilibrated by initial energy minimization and subsequent free relaxation for 100 ps under an NPT ensemble to ensure a constant temperature of 300 K and zero pressure along the axial direction of the nanopillars. After equilibration, all the nanopillars were compressed along their axis directions at 300 K under an NVT ensemble at a constant strain rate of 5×10^8 s^{-1}.

Throughout simulations, periodic boundary conditions were imposed only along the loading direction, while the other directions were set free. During simulations, common neighbor analysis (CNA)[12] was used to identify atom order and defects generated during deformation. The atoms with BCC order are painted in green, while disordered atoms in dislocation cores and/or surfaces are painted red. Dislocation analysis (DXA)[13] was used to characterize the Burgers and line vectors for the dislocations. The atomic stress and strain were calculated by using the virial stress theorem and a local transformation matrix between the current and reference configurations[14,15], respectively.

Text S1. Strengthening slopes for the size effect

The strengthening slopes for the size effect of flow stress in HEA pillars are lower than those for the yield stress. This indicates that the dislocations during the plastic flow stage have a lower mobility than those during the yielding stage, because the dislocation density during the flow stage becomes much higher than that during the yielding stage with increasing plastic strain. Notably, the strengthening slopes for the size effects of yield and flow stresses for single-crystalline HEA pillars exhibit a dependence on orientation, which is related to the motion of screw dislocations activated on different slip planes in the single-crystalline pillars with different orientations.

Text S2. Comparison in deformation behaviors and associated dislocation activities between our HEA micropillars and bulk BCC metals

Early experimental study[16] reported the uniaxial tension and compression of both strain-anneal grown and melt-grown bulk BCC tungsten single crystals with orientations of [001], [110] and [111] in the temperature range of 77-450 K. It was found that multiple slips occur in all three orientations. The experiment results showed that high strain hardening exponent is not related to the accumulation of defects on screw dislocations, but is due to an insufficiently understood process of exhaustion of mobile dislocation[16]. The experiments also indicated that different flow stress in tension and compression of [001]- and [111]-oriented single crystals arise from an anisotropy of lattice friction stress on the {112} planes[16]. The multiple slips in bulk BCC W single crystals are very similar to those in our current experiments in BCC HEA. The activated slip systems during the compression of [001]- and [110]-oriented bulk BCC W single crystals are the same as those in our current experiments in BCC HEA. In bulk BCC W single crystals, the yield strength, flow stress and dislocation slip are dependent on the orientation. These results are consistent with our experimental results of BCC HEA. The main difference between early experiments[16] and our experiments is that our BCC HEA micropillars exhibit the higher strain hardening exponents than bulk BCC W, which is due to the solid solution effects and the smaller sample size in our HEAs. In our experiments, different flow stress in compression of [001]- and [111]-oriented HEA micropillars is mainly related to the activation of different slip systems and different dislocation evolution. This result is essentially attributed to different orientations, which is basically consistent with the early experiments of compression in bulk BCC W single crystals.

Text S3. Deformation twinning in [110]-oriented nanopillars

At a strain of 4.5%, 1/6<111> twinning partial dislocation nucleates from the free surface and then slips on the {112} slip plane (Figure S2a). Subsequently, the continuous nucleation and motion of the next two 1/6<111> twinning partial dislocations along the adjacent {112} slip planes lead to the formation of twin embryos (Figures S2b and 5e). As the applied strain increases, the twin gradually grows with the layer-by-layer migration of the twin boundary (Figures S2c-d and 5f). This twinning process is consistent with that reported during in situ TEM observations for W nanowires[17] and MD simulations of single-crystalline W nanopillars[17]. During deformation, multiple twins nucleate and grow, but only the earliest nucleated twin dominates the plastic deformation, and the other twins are suppressed (Figures S2d and 5f). According to the Schmid factor analyses, deformation twinning should be activated during the compression of [110]-oriented pillars. However, this was found to only occur in our MD simulations and was not observed in our experiments. This phenomenon is related to the strain rate and sample size dependences of deformation twinning and the competition between deformation twinning and dislocation slip. For the compression of single-crystalline BCC metals/alloys, the activation of deformation twinning requires high critical compressive stress[17] (for example, 14-18 GPa for [100]-oriented W[17]). In our MD simulations, both ultrahigh strain rates and very small samples facilitate the achievement of high compression stress (approximately 5.4 GPa for nanopillars with a diameter of 30 nm), which is used to activate deformation twinning. However, in our experiments, the compression strength is relatively low (approximately 1.0-1.7 GPa for [110]-oriented pillars with diameters of 270-1,263 nm) and not enough to activate deformation twinning. Except for the influence of the strain rate and sample size, there are some initial defects on the surface or in the interior of the experimental specimens. These defects give rise to stress concentration, which facilitates dislocation nucleation near these defects, leading to the activation of dislocation slip and further suppression of deformation twinning.

After deformation twinning is activated in simulated [110]-oriented nanopillars (i.e. after plastic yielding), the twin gradually grows up by the continuous slip of partial dislocations along twin boundary. Consequently, the applied stress after yielding rapidly drops to a stress level that only maintains the slip of partial dislocations, leading to the low flow stress in simulated [110]-oriented nanopillars. However, for the experimental [110]-oriented micropillars, the applied stress after yielding is required to drive dislocation interaction, tangle and accumulation. Therefore, the flow stress in experimental [110]-oriented micropillars gradually increases, indicating a significant strain hardening.

Table S1. Energy dispersive spectrum (EDS) results showing the element distribution of dendrite, interdendrite and grain boundary structures

Region	Al	Ni	Cr	Fe	Co
Dendrite	26.65	27.87	11.84	14.88	18.76
Interdendrite	1.90	14.57	33.06	28.05	22.42
Grain boundary	8.31	14.16	27.15	27.44	22.93

Table S2. Schmid factor and the angle between slip plane and loading direction of pillars compressed in [100], [110] and [111] directions

Slip systems		[100] direction		[110] direction		[111] direction	
		Schmid factor	**Angle**	**Schmid factor**	**Angle**	**Schmid factor**	**Angle**
Major slip $\{110\}\langle 111\rangle$	$(110)[\bar{1}11]$	0.408	45 °	—	—	0.272	55 °
	$(110)[1\bar{1}1]$	0.408		—	—	0.272	
	$(1\bar{1}0)[111]$	0.408		—	—	—	—
	$(1\bar{1}0)[11\bar{1}]$	0.408		—	—	—	—
	$(101)[\bar{1}11]$	0.408		—	—	0.272	55 °
	$(101)[11\bar{1}]$	0.408		0.408	30 °	0.272	
	$(10\bar{1})[111]$	0.408		0.408		—	—
	$(10\bar{1})[1\bar{1}1]$	0.408		—	—	—	—
	$(011)[1\bar{1}1]$	—	—	—	—	0.272	55 °
	$(011)[11\bar{1}]$	—	—	0.408	30 °	0.272	
	$(01\bar{1})[111]$	—	—	0.408		—	—
	$(01\bar{1})[\bar{1}11]$	—	—	—	—	—	—
Major slip $\{112\}\langle 111\rangle$	$(112)[11\bar{1}]$	0.236	35 °	0.471	35 °	0.314	70 °
	$(\bar{1}12)[1\bar{1}1]$	0.236		—	—	0.157	28 °
	$(1\bar{1}2)[\bar{1}11]$	0.236		—	—	0.157	
	$(11\bar{2})[111]$	0.236		0.471	35 °	—	—
	$(121)[1\bar{1}1]$	0.236		—	—	0.314	70 °
	$(\bar{1}21)[11\bar{1}]$	0.236		0.236	17 °	0.157	28 °
	$(1\bar{2}1)[111]$	0.236		0.236		—	—
	$(12\bar{1})[\bar{1}11]$	0.236		—	—	0.157	28 °
	$(\bar{2}11)[111]$	0.471	55 °	0.236	17 °	—	—
	$(211)[\bar{1}11]$	0.471		—	—	0.314	70 °
	$(2\bar{1}1)[11\bar{1}]$	0.471		0.236	17 °	0.157	28 °
	$(21\bar{1})[1\bar{1}1]$	0.471		—	—	0.157	
Minor slip $\{123\}\langle 111\rangle$	$(123)[11\bar{1}]$	0.154	16 °	0.463	35 °	0.308	68 °
	$(\bar{1}23)[1\bar{1}1]$	0.154		0.154	11 °	0.206	38 °
	$(1\bar{2}3)[\bar{1}11]$	0.154		0.154		0.103	18 °
	$(12\bar{3})[111]$	0.154		0.463	35 °	—	—

(132)[1 $\bar{1}$ 1]	0.154		—	—	0.308	68 °
($\bar{1}$32)[11 $\bar{1}$]	0.154		0.308	22 °	0.206	38 °
(13 $\bar{2}$)[$\bar{1}$11]	0.154		—	—	0.103	18 °
(1 $\bar{3}$2)[111]	0.154		0.308	22 °	—	—
(213)[11 $\bar{1}$]	0.308	32 °	0.463	35 °	0.308	68 °
(2 $\bar{1}$3)[$\bar{1}$11]	0.308		—	—	0.206	38 °
($\bar{2}$13)[1 $\bar{1}$1]	0.308		—	—	0.103	18 °
(21 $\bar{3}$)[111]	0.308		0.463	35 °	—	—
(231)[1 $\bar{1}$1]	0.308		—	—	0.308	68 °
(23 $\bar{1}$)[$\bar{1}$11]	0.308		—	—	0.206	38 °
($\bar{2}$31)[11 $\bar{1}$]	0.308		0.154	11 °	0.103	18 °
(2 $\bar{3}$1)[111]	0.308		0.154		—	—
(312)[$\bar{1}$11]	0.463	53 °	—	—	0.308	68 °
(3 $\bar{1}$2)[11 $\bar{1}$]	0.463		0.308	22 °	0.206	38 °
(31 $\bar{2}$)[1 $\bar{1}$1]	0.463		—	—	0.103	18 °
($\bar{3}$12)[111]	0.463		0.308	22 °	—	—
(321)[$\bar{1}$11]	0.463		—	—	0.308	68 °
(32 $\bar{1}$)[1 $\bar{1}$1]	0.463		—	—	0.206	38 °
(3 $\bar{2}$1)[11 $\bar{1}$]	0.463		0.154	11 °	0.103	18 °
($\bar{3}$21)[111]	0.463		0.154		—	—

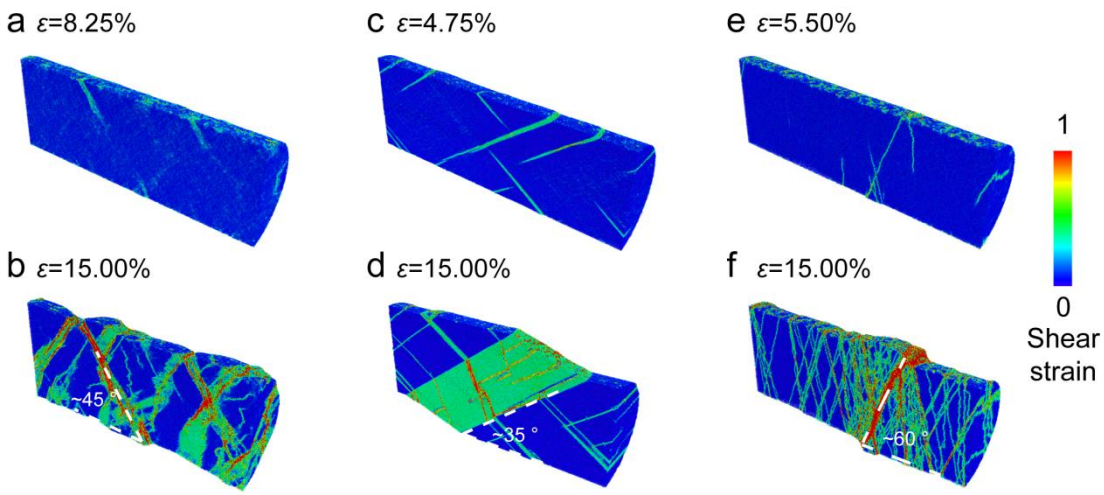

Figure S1. Deformation mechanisms of single-crystalline HEA nanopillars from MD simulations rendered by atomic shear strain. (a-b) A sequence of snapshots of [100]-oriented nanopillars at different compressive strains, showing the activation of multiple slip. (c-d) A sequence of snapshots of [110]-oriented nanopillars at different compressive strains, showing nucleation and growth of deformation twin. (e-f) A sequence of snapshots of [111]-oriented nanopillars at different compressive strains, indicating that dislocation reaction and tangle mainly occur in the distorted region.

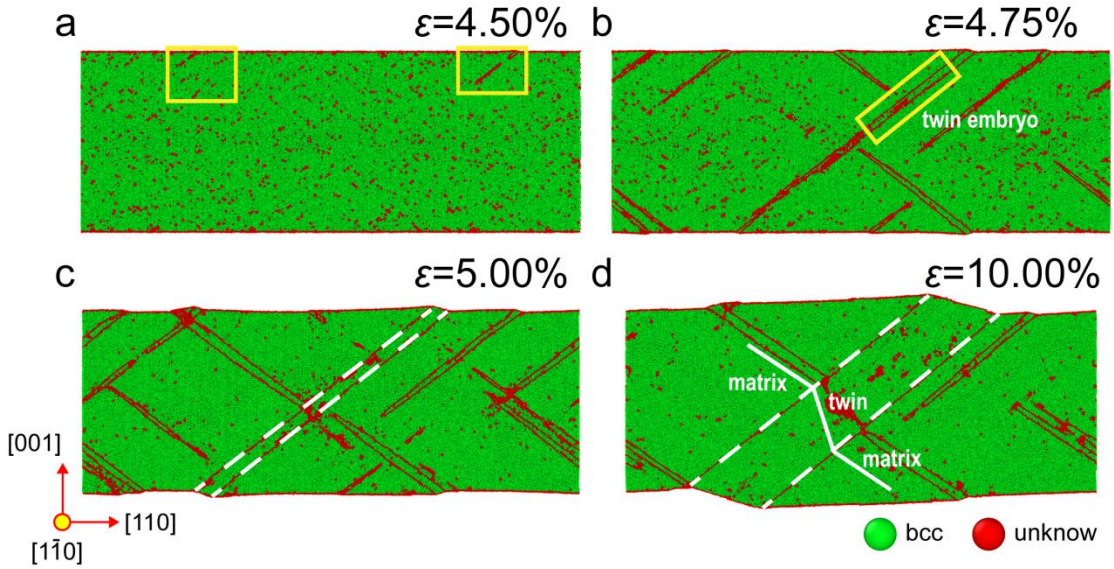

Figure S2. Twin nucleation and growth during compression of [110]-oriented nanopillars with diameter of 30 nm from MD simulations. (a) Dislocation emission from free surface. (b) Formation of twin embryo. (c,d) Twin growth via twin boundary migration.

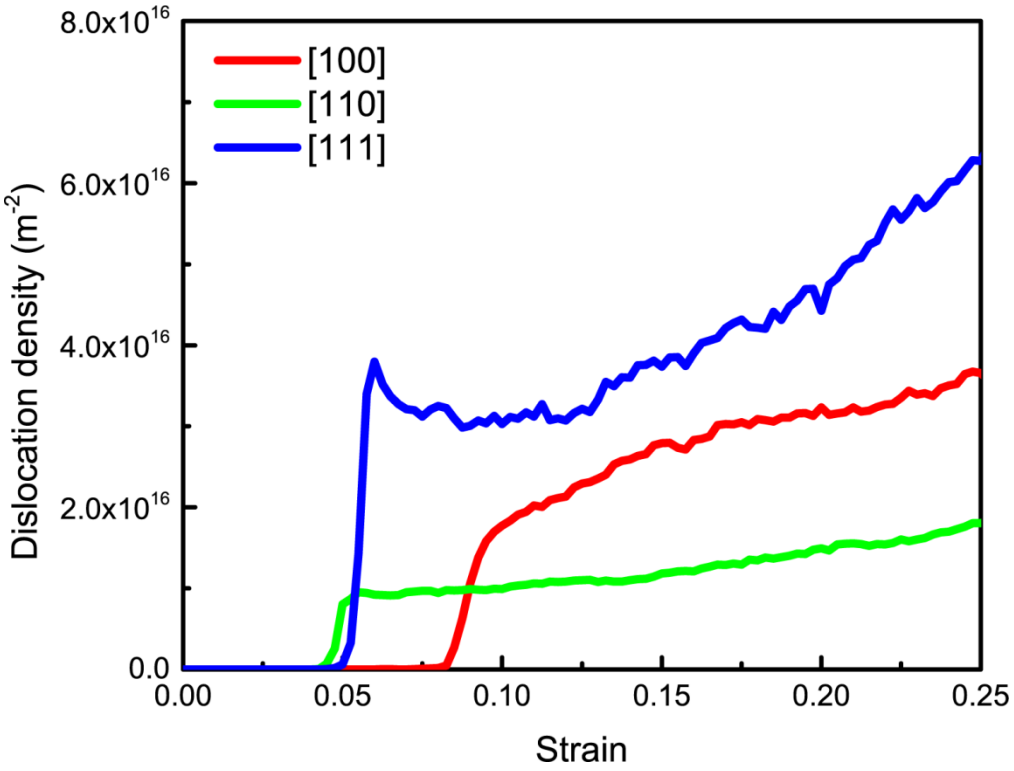

Figure S3. Dislocation density evolution of deformed single-crystalline nanopillars with diameter of 30 nm from MD simulations.

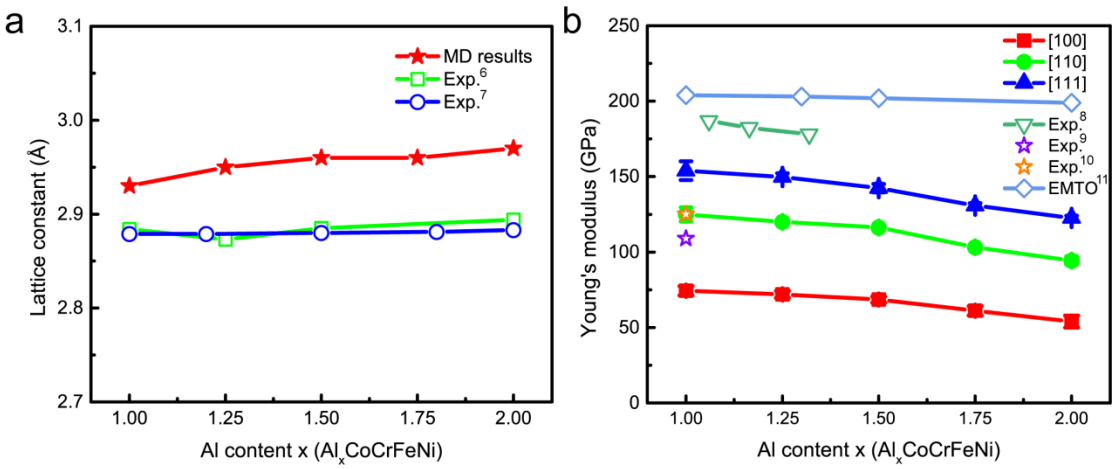

Figure S4. Variations of lattice constants and Young's moduli of $Al_xCoCrFeNi$ with Al content *x* from MD simulations based on the EAM potential we used. (a) Variation of lattice constants with Al content. (b) Variation of Young's moduli of $Al_xCoCrFeNi$ with Al content *x*.

Captions for Videos S1 to S9

Video S1. In situ compression of [100]-oriented nanopillar with D=770 nm. A small slip occurred on top of the pillar. With increasing strain, a second slip appeared at the bottom slip. Both slips induce significant stress drops in the stress-strain curve. The corresponding stress-strain curve is provided on the right side.

Video S2. In situ compression of [110]-oriented nanopillar with D=1015 nm. The nanopillar exhibited several slips on parallel slip planes in the same slipping system during plastic deformation. The corresponding stress-strain curve is provided on the right side.

Video S3. In situ compression of [111]-oriented nanopillar with D=1239 nm. The nanopillar showed obvious multiple slip and continuous strain hardening during the plastic flow stage. The corresponding stress-strain curve is provided on the right side.

Video S4. Atomistic simulation of uniaxial compression on [100]-oriented nanopillar with diameter of 30 nm. Dislocations nucleate from free surface, and then slip on the slip planes and further interact with other dislocations, forming multiple slip bands. Some dislocations escape from free surface, leading to the formation of surface steps.

Video S5. Atomistic simulation of uniaxial compression on [110]-oriented nanopillar with diameter of 30 nm. Nucleation and growth of twins are observed during compression of [110]-oriented nanopillars, indicating that deformation twinning dominates plastic deformation.

Video S6. Atomistic simulation of uniaxial compression on [111]-oriented nanopillar with diameter of 30 nm. Dislocations interact, reaction and tangle dominate the plastic deformation during compression of [111]-oriented nanopillar.

Video S7. Dislocation evolution during uniaxial compression on [100]-oriented nanopillar with diameter of 30 nm. Dislocations nucleate from free surface, and then slip on the slip planes and further interact with other dislocations, forming multiple slip bands. Some dislocations escape from free surface, leading to the formation of surface steps.

Video S8. Dislocation evolution during uniaxial compression on [110]-oriented nanopillar with diameter of 30 nm. Because deformation twinning dominates plastic deformation, leading to the lower dislocation density during compression of [110]-oriented nanopillar.

Video S9. Dislocation evolution during uniaxial compression on [111]-oriented nanopillar with diameter of 30 nm. Dislocations interact, reaction and tangle dominate the plastic deformation during compression of [111]-oriented nanopillar.

References

(1) Oliver, W. C.; Pharr, G. M. An improved technique for determining hardness and elastic-modulus using load and displacement sensing indentation experiments. *J. Mater. Res.* **1992,** *7* (6), 1564-1583.

(2) Plimpton, S. Fast parallel algorithms for short-range molecular-dynamics. *J. Comput. Phys.* **1995,** *117* (1), 1-19.

(3) Zhou, X. W.; Johnson, R. A.; Wadley, H. N. G. Misfit-energy-increasing dislocations in vapor-deposited CoFe/NiFe multilayers. *Phys. Rev. B* **2004,** *69*, 144113.

(4) Onat, B.; Durukanoglu, S. An optimized interatomic potential for Cu-Ni alloys with the embedded-atom method. *J. Phys. Condens. Matter* **2014,** *26* (3), 035404.

(5) Chowdhury, P.; Sehitoglu, H.; Maier, H. J.; Rateick, R. Strength prediction in NiCo alloys–The role of composition and nanotwins. *Int. J. Plast.* **2016,** *79*, 237-258.

(6) Chou, H.-P.; Chang, Y.-S.; Chen, S.-K.; Yeh, J.-W. Microstructure, thermophysical and electrical properties in $Al_xCoCrFeNi$ ($0 \le x \le 2$) high-entropy alloys. *Mater. Sci. Eng. B* **2009,** *163* (3), 184-189.

(7) Wang, W.-R.; Wang, W.-L.; Wang, S.-C.; Tsai, Y.-C.; Lai, C.-H.; Yeh, J.-W. Effects of Al addition on the microstructure and mechanical property of $Al_xCoCrFeNi$ high-entropy alloys. *Intermetallics* **2012,** *26*, 44-51.

(8) Li, M.; Gazquez, J.; Borisevich, A.; Mishra, R.; Flores, K. M. Evaluation of microstructure and mechanical property variations in $Al_xCoCrFeNi$ high entropy alloys produced by a high-throughput laser deposition method. *Intermetallics* **2018,** *95*, 110-118.

(9) Wang, Y. P.; Li, B. S.; Ren, M. X.; Yang, C.; Fu, H. Z. Microstructure and compressive properties of AlCrFeCoNi high entropy alloy. *Mater. Sci. Eng. A* **2008,** *491* (1-2), 154-158.

(10) Zhu, J. M.; Fu, H. M.; Zhang, H. F.; Wang, A. M.; Li, H.; Hu, Z. Q. Synthesis and properties of multiprincipal component $AlCoCrFeNiSi_x$ alloys. *Mater. Sci. Eng. A* **2010,** *527* (27-28), 7210-7214.

(11) Tian, F.; Delczeg, L.; Chen, N.; Varga, L. K.; Shen, J.; Vitos, L. Structural stability of $NiCoFeCrAl_x$ high-entropy alloy fromab initiotheory. *Phys. Rev. B* **2013,** *88*, 085128.

(12) Faken, D.; Jónsson, H. Systematic analysis of local atomic structure combined with 3D computer graphics. *Comput. Mater. Sci.* **1994,** *2* (2), 279-286.

(13) Stukowski, A.; Bulatov, V. V.; Arsenlis, A. Automated identification and indexing of dislocations in crystal interfaces. *Modelling Simul. Mater. Sci. Eng.* **2012,** *20*, 085007.

(14) Falk, M. L.; Langer, J. S. Dynamics of viscoplastic deformation in amorphous solids. *Phys. Rev. E* **1998,** *57* (6), 7192-7205.

(15) Shimizu, F.; Ogata, S.; Li, J. Theory of shear banding in metallic glasses and molecular dynamics calculations. *Mater. Trans.* **2007,** *48* (11), 2923-2927.

(16) Argon, A. S.; Maloof, S. R. Plastic deformation of tunsten single crystals at low temperatures. *Acta Metall.* **1966**, 14, 1449-1462.

(17) Wang, J.; Zeng, Z.; Weinberger, C. R.; Zhang, Z.; Zhu, T.; Mao, S. X. In situ atomic-scale observation of twinning-dominated deformation in nanoscale body-centred cubic tungsten. *Nat. Mater.* **2015,** *14* (6), 594-600.